NF-κB-driven LUZP1 promotes metastasis and chemoresistance in head and neck squamous cell carcinoma

CHEN-YUAN LIN[1,2*], CHING-YUN HSIEH[2,3*], HSIN-CHI LAN[4], CHING-CHAN LIN[2], TZU-TING CHEN[2], WEI-CHI TSENG[2], YUNG-AN TSOU[5,6] and WEI-CHAO CHANG[4]

[1]School of Pharmacy and Graduate Institute, China Medical University, Taichung 406040, Taiwan, R.O.C.; [2]Division of Hematology and Oncology, China Medical University Hospital, Taichung 404327, Taiwan, R.O.C.; [3]Division of Hematology and Oncology, Asia University Hospital, Taichung 413505, Taiwan, R.O.C.; [4]Center for Molecular Medicine, China Medical University Hospital, Taichung 406040, Taiwan, R.O.C.; [5]Department of Otolaryngology-Head and Neck Surgery, China Medical University Hospital, Taichung 404327, Taiwan, R.O.C.; [6]School of Medicine, China Medical University, Taichung 404333, Taiwan, R.O.C.

Received October 3, 2025; Accepted February 24, 2026

DOI: 10.3892/or.2026.9115

Abstract. Head and neck squamous cell carcinoma (HNSCC) remains a highly aggressive malignancy with poor prognosis driven by metastasis and therapeutic resistance. Through comparative proteomic profiling of tumor specimens from patients with long- and short-term survival, the present study identified leucine zipper protein 1 (LUZP1) as one of the most upregulated proteins in tumors from short-term survivors. Functional assays revealed that LUZP1 knockdown impaired migration, invasion, invadopodia formation and epithelial-mesenchymal transition, while enhancing sensitivity to docetaxel and cisplatin. Analysis of paired primary and metastatic tumors further confirmed elevated LUZP1 expression in metastatic sites. Mechanistically, NF-κB inhibition markedly reduced LUZP1 expression, whereas stimulation with IL-1β or TNF-α induced its upregulation and rescued the migration defect caused by LUZP1 depletion, implicating NF-κB as a key upstream regulator. Immunohistochemical analysis of clinical samples demonstrated that high LUZP1 expression was associated with shorter overall and progression-free survival. Collectively, these findings identify LUZP1 as a novel NF-κB-regulated effector that promotes metastasis and chemoresistance and highlight its potential as a prognostic biomarker and therapeutic target in HNSCC.

Correspondence to: Dr Yung-An Tsou, Department of Otolaryngology-Head and Neck Surgery, China Medical University Hospital, 2 Yude Road, Taichung 404327, Taiwan, R.O.C
E-mail: d22052121@yahoo.com.tw

Dr Wei-Chao Chang, Center for Molecular Medicine, China Medical University Hospital, 6F, 350 Jingmao 1st Road, Beitun, Taichung 406040, Taiwan, R.O.C
E-mail: 021443@tool.caaumed.org.tw

*Contributed equally

Key words: head and neck squamous cell carcinoma, leucine zipper protein 1, NF-κB, metastasis, chemoresistance

Introduction

Head and neck squamous cell carcinoma (HNSCC) remains a highly aggressive malignancy characterized by substantial heterogeneity in clinical behavior and treatment response (1). Despite advances in surgical techniques, radiotherapy, chemotherapy and immunotherapy, a substantial proportion of patients still experience poor progression, manifested as local recurrence, distant metastasis, treatment resistance and ultimately reduced survival (2,3). Identifying and validating biomarkers associated with poor progression is therefore of particular importance (4). Such markers not only provide mechanistic insights into tumor aggressiveness and disease evolution but also serve as prognostic tools to stratify patients according to risk. Moreover, survival-related markers can inform personalized treatment strategies, guide therapeutic escalation or de-escalation and support the development of novel targeted interventions (5). The established markers associated with poor progression in HNSCC include human papillomavirus, TP53 mutations, EGFR overexpression, elevated programmed cell death-ligand 1 expression and the upregulation of epithelial-mesenchymal transition (EMT)/stemness-related genes (6-8). These markers are associated with tumor invasion, metastasis, therapeutic resistance and immune evasion. A comprehensive analysis of poor progression markers thus holds considerable promise for improving prognostication, optimizing patient management and advancing precision oncology in HNSCC.

Leucine zipper protein 1 (LUZP1) is a highly conserved cytoskeletal- and signaling-associated protein that plays key roles in the maturation of contractile actomyosin bundle, cytoskeletal organization and the regulation of cell division (9,10). LUZP1 is initially identified in the brain, where it participates in embryonic neural development (11). Emerging evidence

further suggests that LUZP1 exerts vital functions in tumor biology (12-16). Aberrant expression of LUZP1 has been shown to enhance tumor cell migration, invasion and EMT in osteosarcoma and triple-negative breast cancer (12,13). Previous proteomic analyses have also identified LUZP1 as a component of oncogenic signaling networks that contribute to therapeutic resistance (14). Moreover, LUZP1 expression has been associated with poor prognosis in several malignancies, including osteosarcoma, renal papillary cell carcinoma and ovarian cancer (12,15,16). However, the oncogenic role and clinical importance of LUZP1 in HNSCC remain to be elucidated.

The present study first performed a proteomic analysis comparing tumor specimens from patients with HNSCC with favorable long-term survival and those with poor short-term survival. Bioinformatic pathway enrichment was then conducted to identify candidate survival-associated regulators. Based on this discovery-driven approach, the present study aimed to functionally characterize selected candidates *in vitro* and in clinical specimens, and to determine their mechanistic contribution to metastasis, chemoresistance and patient prognosis in HNSCC.

Materials and methods

Pathological tissue specimens. The present study protocol was approved by the Ethics Committee of China Medical University Hospital (approval no. CMUH108-REC1-127). Tumor mass and tumor slice specimens from patients with HNSCC were obtained from the Human Biobank of China Medical University Hospital (Taichung, Taiwan). For proteomic analysis and protein expression validation, three tumor masses from the short-term survival group and three from the long-term survival group were included. Patients with an overall survival of <2 years were classified as the short-term survival group, whereas those with an overall survival of ≥5 years were defined as the long-term survival group. For immunohistochemical analysis, tumor tissue samples from 130 patients enrolled between June 2014 and September 2016 were retrospectively analyzed. The inclusion criteria included i) newly diagnosed squamous cell carcinoma; ii) advanced-stage disease (stage III-IV); and iii) receipt of both radiotherapy and surgical treatment. Specimens were excluded if patients i) had documented HIV infection or ii) declined to provide informed consent for tissue use.

The demographic and clinicopathological characteristics of the HNSCC cohort are summarized in Table I. Pathological tissue specimens were primarily obtained from tumors of the oral cavity, tongue and oropharynx. In addition, one paired set of tumor slices derived from the primary tumor and lymph node metastasis of the same patient was also included in the analysis.

In silico analyses. LUZP1 gene expression levels between normal tissue and primary tumor, as well as across different nodal metastasis statuses, were analyzed using the UALCAN web platform based on The Cancer Genome Atlas (TCGA) database (17). Pairwise gene expression correlation analyses were conducted using the Gene Expression Profiling Interaction Analysis (GEPIA) web server, (http://gepia.cancer-pku.cn/), which integrates TCGA and Genotype Tissue Expression data processed through a standardized analytical pipeline (18). The monotonic associations between LUZP1 and NFKB1 or NFKB2 expression levels were evaluated using Spearman's rank correlation coefficient. ChIP-seq bioinformation of cell lines was obtained from the Encyclopedia of DNA Elements (ENCODE) project database (https://www.encodeproject.org/). ENCODE cell lines are well-characterized and publicly available cell models that have undergone extensive validation, including authentication and quality control assessments. Data were accessed through the ENCODE portal and used in accordance with the project's data usage guidelines.

Cell lines and cell culture. The human pharyngeal squamous cell carcinoma cell line FaDu (cat. no. HTB-43) was obtained from the American Type Culture Collection. The human oral squamous carcinoma cell line OECM-1 (cat. no. SCC180) was purchased from Merck KGaA and the human tongue squamous cell carcinoma cell line SAS (cat. no. JCRB0260) was obtained from Japanese Collection Research Bioresources Cell Bank. FaDu cells were maintained in Dulbecco's Modified Eagle Medium (DMEM; cat. no. 12100046; Gibco; Thermo Fisher Scientific, Inc.); OECM-1 cells were cultured in RPMI-1640 medium (cat. no. 31800022; Gibco; Thermo Fisher Scientific, Inc.) supplemented with 2 mM l-glutamine (cat. no. 5-10K00-H; BioConcept Ltd.), while SAS cells were maintained in DMEM supplemented with 2 mM l-glutamine. Docetaxel-resistant (DTXr) and cisplatin-resistant (CISr) OECM-1 cell lines were established by continuous exposure to DTX (0.2 nM; cat. no. BML-T129; Enzo Life Sciences) and CIS (0.5 μM; cat. no. 232120 Merck KGAa) for 3 months, which gradually enhanced their chemoresistance. All cells were maintained in a humidified incubator with 5% CO_2 and 95% air at 37˚C.

Chemical reagents and treatments. HNSCC cell lines (FaDu, OECM-1 and SAS) were treated with pharmacological inhibitors and cytokines to evaluate their effects on LUZP1 expression. The pharmacological inhibitors used in the present study included SB431542 (5 and 10 μM; cat. no. 616464; Merck KGaA), LY294002 (5 and 10 μM; cat. no. HY-10108; MedChemExpress), rapamycin (5 and 10 μM; cat. no. R0395; Merck KGaA), BAY 11-7085 (5 and 10 μM; cat. no. HY-10257; MedChemExpress), and YC-1 (10 and 30 μM; cat. no. sc-202856; Santa Cruz Biotechnology, Inc.). Cytokine treatments included IL-1β (3 ng/ml; cat. no. C01002-100UG; Croyez Bioscience Co., Ltd.) and TNFα (10 ng/ml; cat. no. C01047-100UG; Croyez Bioscience Co., Ltd.). Cells were incubated with the indicated inhibitors or cytokines at 37˚C for 24 h unless otherwise specified. For time-course analysis of LUZP1 induction, cells were treated with IL-1β (3 ng/ml) for 0, 1, 4 and 24 h or with TNFα (10 ng/ml) for 0, 6 and 24 h. In addition, TNFα (10 ng/ml) was applied to OECM-1 cells to assess its effects on tumor cell migration. Cell migratory capacity was assessed using a Transwell migration assay, as described in the *Transwell migration and invasion assays* section.

Transwell migration and invasion assays. For the *in vitro* migration assay, tumor cells ($2x10^4$ cells in 200 μl of media) were seeded into the upper chamber of a polyethylene terephthalate

Table I. Demographic characteristics of patients with head and neck squamous cell carcinoma.

Characteristics	n	%
Sex		
Male	121	93.1
Female	9	6.9
Age		
<40	28	26.5
40-60	79	60.8
>60	23	17.7
Site		
Buccal mucosa	49	37.7
Tongue	49	37.7
others	32	24.6
T		
1	14	10.8
2	45	34.6
3	25	19.2
4	46	35.4
NS		
0	44	33.8
1	15	11.5
2	47	36.2
3	24	18.5
Differentiation		
Well	54	41.5
Moderate	58	44.6
Poor	18	13.8
PNI		
Y	67	51.5
N	63	48.5
LVI		
Y	48	36.9
N	82	63.1
ENE		
Y	36	27.7
N	50	38.5
Nodal negative	44	33.8

T, tumor stage; NS, nodal stage; PNI, perineural invasion; LVI, lymphovascular invasion; ENE, extranodal extension; Y, yes; N, no.

membrane Transwell insert (cat. no. 353097; Corning, Inc.) placed on a 24-well plate. For the *in vitro* invasion assay, tumor cells ($4x10^4$ cells in 200 μl of media) were seeded into the upper chamber of Transwell inserts precoated (at 37˚C for 24 h) with Matrigel (1 g/l; cat. no. 356234; BD Biosciences). Serum-free media was added to the upper chamber, while medium supplemented with 10% FBS (Corning, Inc.) was added into the lower chamber as a chemoattractant. After incubation at 37˚C for 24 h (for migration assay) or 48 h (for invasion assay), the cells that migrated or invaded through the membrane were fixed with 3.7% formalin (10 min; room temperature; cat. no. 15512; Merk KGAa) and stained with 0.1% crystal violet (30 min; room temperature; cat. no. C0775; Merck KGAa). The stained cells were destained with 50% ethanol (30 min; room temperature; cat. no. 459836; Merck KGAa) and 0.1% acetic acid (cat. no. A6283; Merck KGAa), and then the absorbance of the extracted dye was measured spectrophotometrically at 570 nm for quantification and cell images were acquired using a bright-field light microscope.

Three-dimensional (3D) tumor spheroid invasion assay. Cells (3,000 cells per well) were seeded into ultra-low attachment (ULA) 96-well round-bottom plates and cultured for 3 days to allow spheroid formation. After spheroids were established, a 3D invasion assay was performed. Growth factor-reduced Matrigel (cat. no. 354230; Corning, Inc.) was diluted in serum-free DMEM to obtain a 2x working concentration. The Matrigel solution was added to pre-chilled ULA 96-well round-bottom plates containing the spheroids at a final volume of 100 μl per well, resulting in a final Matrigel concentration of 3.75 mg/ml. Plates were then incubated at 37˚C for 1 h to allow Matrigel polymerization. 3D tumor spheroid invasion was quantified using a radial outgrowth distance approach. Phase-contrast images were acquired at 0, 24, 48 and 96 h following spheroid embedding using a Nikon TS100 inverted bright-field light microscope. For each spheroid, the invasion front radius (RX) at each time point was determined by measuring the radial distance from the spheroid center to the outer boundary of the contiguous invading cell population. To minimize the influence of isolated cells and image noise, the invasion front was defined as the 95th percentile (p95) of radial distance measurements obtained along multiple angular axes. The baseline spheroid radius at 0 h (R0) was defined using the same p95 criterion. Invasion distance at each time point was calculated as D=RX–R0. Spatial measurements were converted from pixels to micrometers using the scale bar provided in the 0 h images. All image analyses were performed using ImageJ software (version, 1.54 g; National Institutes of Health) and individual spheroids were analyzed independently as biological replicates for statistical analysis.

Colony formation assay. For the colony formation assay, tumor cells with or without LUZP1 knockdown (1,000 cells per well) were seeded into 6-well plates and cultured for 10 days to allow colony formation. A colony was defined as a cluster containing ≥50 cells. The resulting colonies were fixed with 3.7% formalin (10 min; room temperature) and stained with 0.1% crystal violet (30 min; room temperature). For quantitative analysis, the bound dye was solubilized using 50% ethanol containing 0.1% acetic acid, and the absorbance was measured spectrophotometrically at 570 nm.

Cell viability assay. The effects of chemotherapeutic agents, DTX and CIS, on cell viability were assessed using the methylthiazol MTT method. Tumor cells were seeded in 24-well plates at a density of $2x10^4$ cells per well and treated with DTX (0, 1, 5 and 10 nM) for 48 h or CIS (0, 5, 10 and 20 μM) for 24 h at 37˚C. Following treatment, 200 μl of MTT solution [3-(4,5-dimethylthiazol-2-yl)-2,5-diphenyltetrazolium bromide (cat. no. M6494; Invitrogen; Thermo

Fisher Scientific, Inc.); 1 g/l in PBS] was added to each well and incubated at 37˚C for 4 h. The resulting formazan crystals were solubilized in DMSO (cat. no. C6164, Merck KGAa), and absorbance was measured at 570 nm using an enzyme-linked immunosorbent assay reader (DYNEX® Technologies). Cell viability (%) was calculated as (T/U) x 100, where T represents the absorbance of treated cells and U represents absorbance of untreated cells.

Western blot assay. Total protein lysates from homogenized tumor tissues or cultured cells were extracted using RIPA lysis and Extraction buffer (cat. no. 89901; Thermo Fisher Scientific, Inc.) supplemented with a proteinase inhibitor cocktail (cat. no. 11836170001; Roche Diagnostics GmbH). Protein concentrations were quantified using the Protein Assay kit (cat. no. 5000006EDU; Bio-Rad Laboratories, Inc.) by measuring absorbance at 595 nm. Equal amounts of protein (20 μg) were resolved by 9.5% SDS-PAGE gels and transferred onto PVDF membranes (cat. no. 88518; Thermo Scientific, Inc.) at 400 mA for 3 h. Membranes were blocked with 5% skimmed milk in TBS-0.05% Tween (TBST) for 1 h at room temperature, and incubated with primary antibodies at 4˚C for 16-24 h. The primary antibodies used were as follows: Anti-LUZP1 (1:1,000; cat. no. 17483-1-AP; Proteintech Group, Inc.), anti-E-cadherin (2,000; cat. no. 3195; Cell Signaling Technology, Inc.), anti-vimentin (2,000; cat. no. 3932; Cell Signaling Technology Inc.) and anti-β-actin (10,000; cat. no. 4970; Cell Signaling Technology, Inc.). After three washes with TBST (15 min each), membranes were incubated with horseradish peroxidase-conjugated secondary antibody, peroxidase AffiniPure Goat Anti-Rabbit IgG (H+L) (10,000; cat. no. 111-035-144; Jackson ImmunoResearch Laboratories, Inc.) at room temperature for 1 h. Immunoreactive bands were visualized using an enhanced chemiluminescence substrate (Western Lighting Plus ECL; cat. no. 0RT2655, PerkinElmer, Inc.) and captured with an ImageQuant LAS 4000 luminescence image system (Cytiva). Original western blot images are provided in Table SI.

Chromatin immunoprecipitation followed by quantitative PCR (ChIP-qPCR). ChIP-qPCR was performed to assess NF-κB p65 (RelA) occupancy at selected genomic loci in OECM-1 cells using the SimpleChIP Enzymatic Chromatin IP Kit (Magnetic Beads) (cat. no. 9003; Cell Signaling Technology, Inc.). OECM-1 cells were cultured under standard conditions, stimulated with TNF-α (10 ng/ml; cat. no. C01047-100UG; Croyez Bioscience Co., Ltd.) for 24 h. Cells were cross-linked with 1% formaldehyde at room temperature for 10 min and quenched with glycine. Nuclei were isolated, and chromatin was enzymatically digested with micrococcal nuclease at 37˚C for 25 min, followed by sonication (40 kHz on ice) using eight cycles of 20 s ON and 30 s OFF to generate chromatin fragments ranging from 150 to 900 bp, as confirmed by 1% agarose gel electrophoresis. A 2% aliquot of sheared chromatin was processed in parallel as an input control. For immunoprecipitation, 10 μg of chromatin was incubated overnight at 4˚C with 5 μl of ChIP-grade anti-NF-κB p65 antibody (cat. no. 8242; Cell Signaling Technology, Inc.). Immunoprecipitation with an anti-histone H3 antibody (cat. no. 4620; Cell Signaling Technology, Inc.) was included as a positive control. Immune complexes were captured using ChIP-grade Protein G magnetic beads (cat. no. 9006; Cell Signaling Technology, Inc.) and subjected to sequential low-salt and high-salt washes. Bound chromatin was eluted and reverse cross-linked at 65˚C for 2 h in the presence of proteinase K, followed by DNA purification using spin columns and elution in DNA elution buffer. qPCR was performed using a QuantStudio 5 Real-Time PCR System (Applied Biosystems, Thermo Fisher Scientific, Inc.) with KAPA SYBR FAST qPCR Master Mix (cat. no. KM4106; Roche Diagnostics). Each reaction contained 1 μl of ChIP or input DNA in a total volume of 10 μl. Technical triplicates were averaged and enrichment was calculated as a percentage of input using ΔCq normalization (19) with adjustment for the 2% input dilution. Information of qPCR primers is provided in Table SII.

Gene knockdown by shRNA. Lentiviral plasmids pCMV-ΔR8.91 and pMD.G, along with specific short hairpin RNA (shRNA) constructs in the pLKO.1 vector, were obtained from the National RNAi Core Facility, Academia Sinica. A GFP-targeting shRNA (cat. no. 30323; pLKO.1 GFP shRNA) was used as a control and was purchased from Addgene, Inc. The shRNA sequences used in this study are listed in Table SIII. For lentivirus production, HEK293T cells were transiently co-transfected with the shRNA expression plasmid and the packaging plasmids pCMV-ΔR8.91 and pMD.G at a plasmid ratio of 4 μg:3.6 μg:0.4 μg (shRNA:pCMV-ΔR8.91:pMD.G). Plasmid DNA was mixed with Lipofectamine® 2000 (Invitrogen; Thermo Fisher Scientific, Inc.) and incubated at RT for 20 min to allow complex formation, followed by transfection, according to the manufacturer's instructions. A total of 48 h after transfection at 37˚C, the viral supernatants were collected, filtered through a 0.22 μm membrane filter, and used for subsequent infection. HNSCC cells were infected with shRNA-containing viral supernatant in the presence of polybrene (8 μg/ml). After 24 h of incubation at 37˚C, the medium was replaced with fresh complete medium containing puromycin (2 μg/ml) for 2 weeks for selection. Cells were maintained under puromycin selection and harvested for downstream analyses as indicated in each experiment.

Immunofluorescent analysis. Tumor cells cultured on cover glasses or in 6-well plates were rinsed three times with PBS and fixed in 4% formaldehyde (cat. no. 1.04003; Merck KGAa) at room temperature for 7 min. Following fixation, cells were washed three times with PBS (5 min each). Permeabilization was performed with 0.1% Triton X-100 (cat. no. T8532; Merck KGAa) in PBS for 7 min, at room temperature, followed by three additional PBS washes. Non-specific binding was blocked with 1% BSA in PBS at room temperature for 1 h or at 4˚C overnight. Tumor cells were then incubated with LUZP1 antibodies (1:100 dilution in 1% BSA/PBS; cat. no. 17483-1-AP, Proteintech Group Inc.) at room temperature for 1 h, washed and subsequently incubated with fluorophore-conjugated secondary antibodies (1:400 dilution in 1% BSA/PBS; cat. no. A-11008, Thermo Fisher Scientific, Inc.) at room temperature in the dark for 1 h. F-actin was visualized by staining with fluorescent phalloidin (1:200 dilution in 1% PBS; cat. no. R415; Invitrogen; Thermo Fisher Scientific, Inc.) at room temperature in the dark for 30 min. After three final

PBS washes, cover glasses were mounted onto slides using DAPI-containing mounting medium (cat. no. 20004; AAT Bioquest, Inc.), sealed with nail polish and stored at 4˚C until imaging. Fluorescent images were acquired using a fluorescence microscope (Nikon Corporation).

Immunohistochemical analysis. Formalin-fixed, paraffin-embedded clinical tissue specimens were sectioned at 4-μm thickness and baked at 60-65˚C for 1 h, followed by a 10 min cooling step. Slides were deparaffinized twice in xylene (cat. no. 4312, Muto Pure Chemicals Co. Ltd.) 10 min each and rehydrated through a graded ethanol series (cat. no. 459836, Merck KGAa; 100, 95, 75 and 50%; 5 min each), then rinsed in double distilled H_2O for 5 min. Heat-induced epitope retrieval was performed in either Tris buffer (pH 9.0; cat. no. 920p-06, Merck KGAa) or citrate buffer (pH 6.0; cat. no. CBB500; ScyTek Laboratories, Inc.) under pressure at 95-100˚C for 15 min, followed by cooling at room temperature for 30 min. Endogenous peroxidase activity was quenched with 3% hydrogen peroxide (cat. no. 31642, Thermo Fisher Scientific Inc.) for 10 min and sections were washed three times with PBS (10 min each). After blocking with 5% normal goat serum (cat. no. 005-000-121; Jackson ImmunoResearch Laboratories, Inc.) for 1 h at room temperature, slides were incubated overnight at 4˚C with anti-LUZP1 primary antibody (1:15 dilution; cat. no. 17483-1-AP, Proteintech Group Inc.). Following three PBS washes, sections were incubated with biotinylated goat anti-rabbit IgG (1:400; cat. no. BA-1000; Vector Laboratories, Inc.) at room temperature for 1 h, and signal amplification was performed using the ABC-HRP kit (cat. no. K-6100; Vector Laboratories, Inc.). Visualization was achieved with Gill's hematoxylin (cat. no. 3801520, Leica Biosystems) for nuclear counterstaining. Finally, slides were dehydrated through graded ethanol (cat. no. 459836; Merck KGAa; 75, 95 and 100%; 3 min each), cleared in xylene (cat. no. 4312, Muto Pure Chemicals Co. Ltd.) 10 min twice and mounted with coverslips. Immunohistochemical images were acquired using a Zeiss Axio Imager Z2 upright fluorescence microscope (Duke) and quantitative analysis was conducted using Tissue FAXS cell analysis software (version, 7.1; Tissuegnostics). The immunohistochemical signals were scored as 0, 1, 2 and 3, and a score ≥2 indicated positive detection.

Proteomic analysis. Total protein extracts (20 μg per sample) were separated on a 9.5% SDS-PAGE gel and divided into four gel fractions for in-gel tryptic digestion as previously described (20). Peptide mixtures were analyzed using an Orbitrap Exploris 480 mass spectrometer (Thermo Scientific, Inc.) coupled with an Ultimate 3000 RSLC nano-liquid chromatography system (Thermo Scientific, Inc.) equipped with a nanospray ionization source (Thermo Scientific, Inc.). Mass spectrometric analyses were performed in positive ion mode under data-dependent acquisition settings. Full mass spectrometry survey scans were acquired in the m/z range of 375-1,500 with an automatic gain control (AGC) target of $4x10^5$ and a resolution of 120,000 at m/z 200. The twenty most abundant multiple-charged precursor ions were sequentially fragmented by collision-induced dissociation and the tandem mass was analyzed in the Orbitrap at a resolution of 30,000. Protein identification and label-free quantification were conducted using Proteome Discovery software (version, 2.4; Thermo Scientific, Inc.), with the identification threshold set at $P<0.05$. Label-free quantification was conducted using Proteome Discoverer version 2.4 (Thermo Fisher Scientific, Inc.) incorporating the Minora feature detection algorithm. Quantitative analysis was based on the peak abundances of precursor ions corresponding to the identified peptides. Proteins exhibiting significant upregulation in the experimental group were subjected to identify significantly enriched biological pathways by Kyoto Encyclopedia of Genes and Genomes (KEGG) pathway enrichment analysis in the DAVID website (https://davidbioinformatics.nih.gov/).

Statistical analysis. All data are presented as the means ± SD. Statistical significance between two independent groups was assessed using a two-tailed unpaired Student's t-test, whereas comparisons among multiple groups were performed using one-way analysis of variance (ANOVA) followed by Tukey's post hoc test. One-to-many comparisons were conducted using one-way ANOVA followed by Dunnett's post hoc test. A factorial two-way ANOVA was performed to assess the effects of two independent variables, followed by Tukey's honestly significant difference post hoc test for multiple comparisons among groups. Correlations between gene expression levels were assessed using Spearman's rank correlation coefficient. Overall survival (OS) and progression-free survival (PFS) were analyzed using the Kaplan-Meier method, and differences between survival curves were evaluated by the log-rank test. All statistical analyses were conducted using SPSS Statistics software (version, 22.0; IBM, Corp.). $P<0.05$ was considered to indicate a statistically significant difference.

Results

LUZP1 is highly expressed in HNSCC tumor tissues with short-term survival. To identify protein signatures potentially associated with poor prognosis, a comparative proteomic analysis of tumor tissues from patients with HNSCC was performed with long- and short-term survival. Patients with an overall survival of <3 years were classified as the short-term survival group, whereas those with an overall survival of ≥5 years were defined as the long-term survival group. Among the 4,246 proteins identified, 187 exhibited a ≥4-fold increase in abundance in short-term survival compared with long-term survival tissues (Table SIV). KEGG pathway enrichment analysis revealed that these upregulated proteins were primarily associated with pathways related to fluid shear stress, drug metabolism, glutathione metabolism and chemical carcinogenesis (Fig. 1A). Fluid shear stress is associated with the metastatic dissemination of tumor cells within the circulatory system (21), whereas drug metabolism is associated with increased therapeutic resistance (22). These findings suggest that tumor metastasis and treatment resistance may represent key determinants underlying poor prognosis and short-term survival in patients with HNSCC. Differential protein expression between short- and long-term survival tissues was visualized using a proteomic volcano plot (Fig. 1B), where the x-axis represents the $\log_2$ fold change in protein abundance and the y-axis represents the $-\log_{10}$ p-value, indicating statistical significance. LUZP1

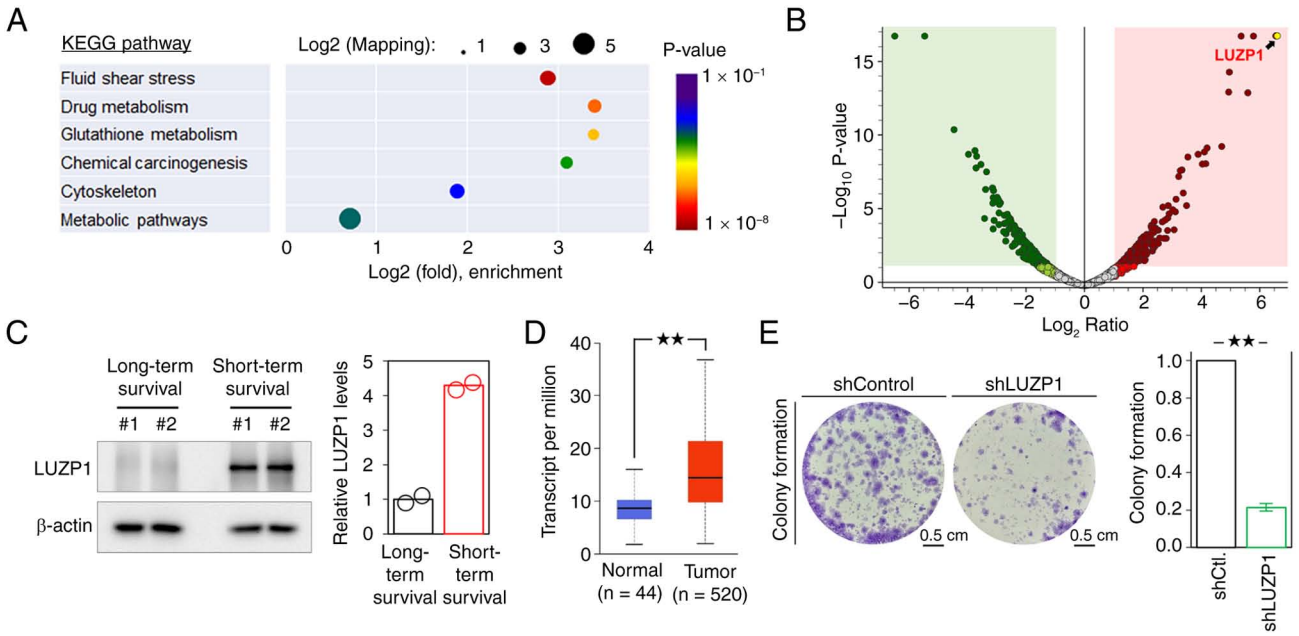

Figure 1. LUZP1 is highly expressed in HNSCC tumor tissues with short-term survival. (A) KEGG pathway annotation of differentially upregulatory proteins identified from the proteomic analysis of tissue specimens of patients with HNSCC with short-term survival compared with long-term survival. The circle size indicates the number of mapping proteins in each process, and the color indicates the P-value of each pathway. (B) Differential protein expression between short- and long-term survival tissues using a proteomic volcano plot. The x-axis represents the $\log_2$ fold change in protein abundance and the y-axis represents the $-\log_{10}$ P-value, indicating statistical significance. The arrow indicated LUZP1 as one of the most upregulated proteins in the short-term survival specimen. (C) The expression of LUZP1 in both long- and short-term survival specimen was determined by western blot assay. Signal quantification was measured using ImageJ 1.54 g software (National Institutes of Health) and the relative intensity was normalized to the long-term survival specimen group (n=2). β-actin, loading control. (D) The relative LUZP1 mRNA levels between HNSCC tissues and normal tissues were analyzed on the UALCAN website using The Cancer Genome Atlas database. (E) Colony formation assay in OECM-1 cells with or without LUZP1 knockdown. Signal quantification using crystal violet extract was measured by colorimetric analysis at 570 nm. The relative signal intensities were normalized to the shControl (n=3). (E) Data are displayed as the means ± SD. For statistical analysis, (A-C) one-way ANOVA followed by Dunnett's post hoc. **P<0.01. LUZP1, leucine zipper protein 1; HNSCC, head and neck squamous cell carcinoma; KEGG, Kyoto Encyclopedia of Genes and Genomes; sh, short hairpin; Ctl., control.

emerged as one of the most upregulated proteins in tumor tissues of patients with HNSCC with short-term survival (Fig. 1B; Table SIV). The elevated expression of LUZP1 was further confirmed in additional tumor specimens by western blot analysis (Fig. 1C). The LUZP1 mRNA expression level of HNSCC tissues was significantly higher when compared with that in the normal tissues via the UALCAN database (Fig. 1D), which provides an in-depth analysis of gene expression data from TCGA (17). Additionally, LUZP1 gene knockdown by shRNA significantly impaired the colony formation of OECM-1 cells (Fig. 1E), suggesting that LUZP1 could enhance the capacity for unlimited proliferation of HNSCC cells (23).

LUZP1 enhances the metastatic abilities of HNSCC cells. Since LUZP1 may contribute to HNSCC metastasis, its effects on the metastatic properties of HNSCC cells was examined. A one-way ANOVA analysis of the Transwell assays revealed a significant difference among Control, shLUZP1#1 and shLUZP1#2 groups (migration: $F(2,6)=142.71$, $P=9.0\times10^{-6}$; invasion: $F(2,6)=193.09$, $P=4.0\times10^{-6}$). Post hoc comparisons using Dunnett's test demonstrated that both shLUZP1#1 and shLUZP1#2 were significantly different from the Control group (shLUZP1#1 vs. Control, $P=1.14\times10^{-4}$; shLUZP1#2 vs. Control, $P=1.82\times10^{-4}$), indicating that knockdown markedly reduced the migration and invasion abilities of HNSCC cells (Fig. 2A and B). Transwell assays demonstrated that LUZP1 knockdown markedly attenuated cell migration and invasion (Fig. 2A and B). 3D tumor spheroid invasion assay was conducted to validate the role of LUZP1 in regulating tumor metastatic abilities. A one-way ANOVA revealed a significant difference among Control, shLUZP1#1 and shLUZP1#2 groups ($F(2,6)=74.81$, $P=5.7\times10^{-5}$). Dunnett's post hoc test demonstrated that both shLUZP1#1 and shLUZP1#2 were significantly reduced compared with the Control group (shLUZP1#1 vs. Control, $P=2.6\times10^{-4}$ and shLUZP1#2 vs. Control, $P=1.1\times10^{-4}$), indicating that LUZP1 knockdown significantly attenuated the invasive capacity of tumor spheroids (Fig. 2C), consistent with the previous two-dimensional migration and invasion assays (Fig. 2A and B). In addition, LUZP1 knockdown reduced the formation of invadopodia-like protrusive structures (Fig. 2D), visualized by phalloidin staining of the key cytoskeletal component F-actin (24). Furthermore, LUZP1 knockdown increased the expression of the epithelial marker E-cadherin while decreasing the expression of the mesenchymal marker vimentin (Fig. 2E), suggesting a role for LUZP1 in promoting EMT. Moreover, analysis of paired primary tumors and metastatic sites from the same patients with HNSCC revealed markedly increased LUZP1 expression in metastatic lesions compared with their matched primary tumors (Fig. 2F). This observation further supports the notion that LUZP1 enhances the metastatic potential of HNSCC cells.

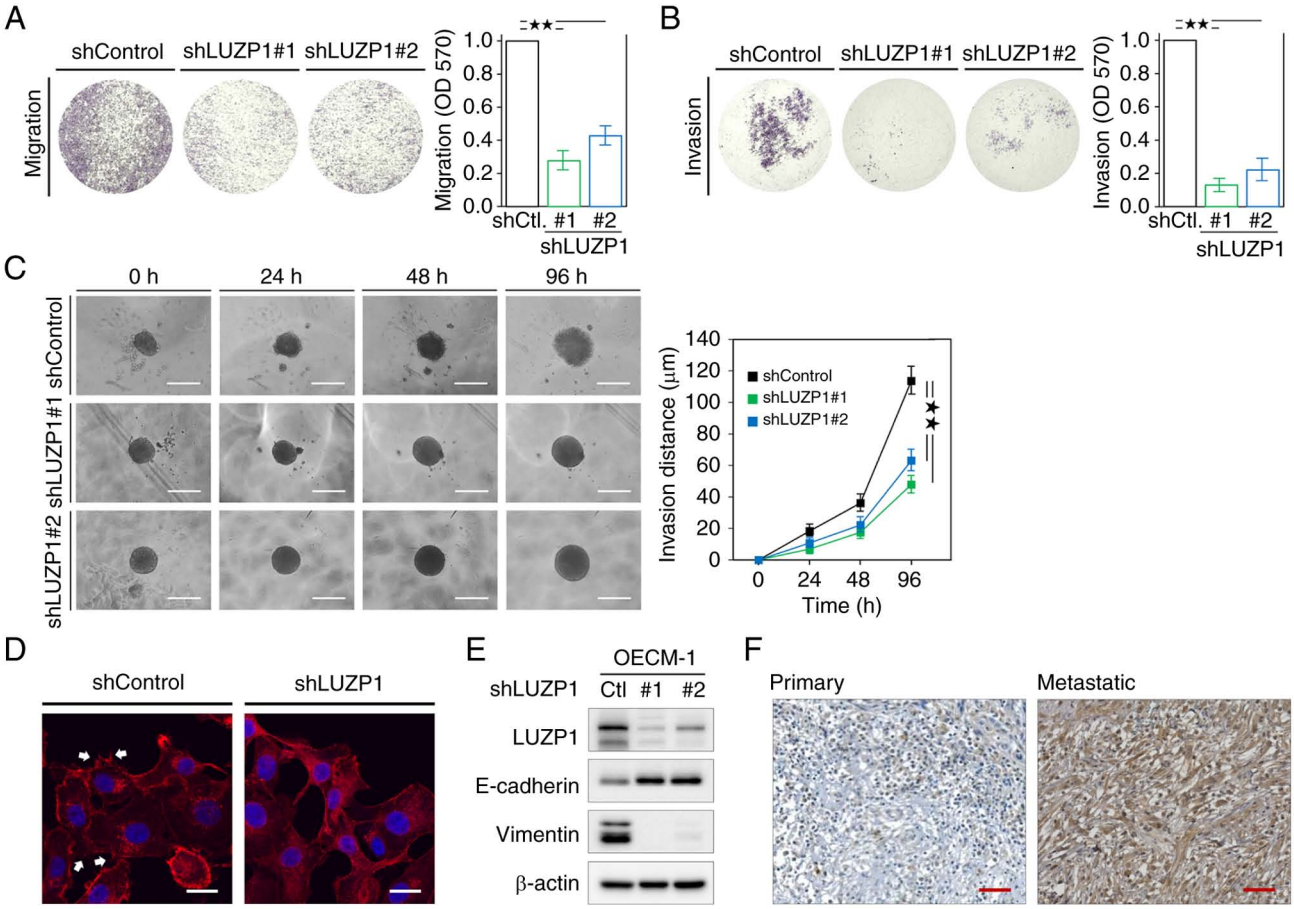

Figure 2. LUZP1 enhances the metastatic abilities of HNSCC cells. (A) cell migration and (B) invasion assay in OECM-1 cells with or without LUZP1 knockdown. Signal quantification using crystal violet extract was measured by colorimetric analysis at 570 nm. The relative signal intensities were normalized to the shControl (n=3). (C) The representative images for 3D invasion assay for tumor spheroids in SAS cells with or without LUZP1 knockdown. A radial outgrowth distance approach is used for quantification of 3D tumor spheroid invasion. Scale bar, 500 μm. (D) Invadopodia-like protrusive structures were visualized by F-actin staining using phalloidin (cat. no. R415; Invitrogen; Thermo Fisher Scientific, Inc.), which are indicated by the arrow. Scale bar, 20 μm. (E) The expression of LUZP1, E-cadherin and vimentin in OECM-1 cells with or without LUZP1 knockdown was determined by western blot assay. β-actin, loading control. (F) The expression of LUZP1 in both primary and metastatic tumors of a patient with HNSCC was examined using immunohistochemical analysis. Scale bar, 50 μm. Data are shown as the means ± SD. For statistical analyses, (A and B) a 2-tailed unpaired Student's t-test; (C) one-way ANOVA with Tukey's post hoc test. **P<0.01. LUZP1, leucine zipper protein 1; HNSCC, head and neck squamous cell carcinoma; sh, short hairpin; Ctl., control.

LUZP1 increases chemoresistance of HNSCC cells. KEGG pathway analysis of upregulated proteins identified in tumor tissues from short-term survival patients with HNSCC revealed significant enrichment of pathways associated with increased therapeutic resistance (Fig. 1A). This prompted the investigation of whether elevated LUZP1 expression contributes to enhanced chemoresistance in HNSCC. To this end, DTXr and CISr OECM-1 cell lines were established by continuous exposure to DTX or CIS, two chemotherapeutic agents commonly used in HNSCC treatment (25). Immunofluorescence analysis demonstrated that LUZP1 expression was markedly elevated in both OECM-1/DTXr and OECM-1/CISr cells compared with their parental counterparts (Fig. 3A). Furthermore, MTT assays revealed that LUZP1 knockdown increased the sensitivity of OECM-1 and SAS cells to DTX and CIS (Fig. 3B and C), indicating that LUZP1 may play a functional role in mediating chemoresistance in HNSCC.

NF-κB signaling activation promotes LUZP1 expression in HNSCC cells. Based on the aforementioned findings, the signaling pathways associated with metastasis and chemoresistance that may regulate LUZP1 expression were investigated using pathway-specific inhibitors. A total of five inhibitors were employed in the present study, including SB431542 for the TGF-β/Smad pathway, LY294002 for PI3K/AKT/mTOR signaling, Rapamycin for mTOR, BAY 11-7085 for NF-κB signaling and YC-1 for the HIF-1 pathway. Semi-quantitative western blot analysis demonstrated that BAY 11-7085 exerted the most pronounced inhibitory effect on LUZP1 expression across all three HNSCC cells (FaDu, OECM-1 and SAS; Fig. 4A), and repeated treatments with BAY 11-7085 consistently reproduced this inhibitory effect on LUZP1 protein levels (Fig. 4B). These results suggest that LUZP1 expression may be regulated by NF-κB signaling activation. Consistently, *in silico* analysis using the GEPIA database revealed a significant positive correlation between LUZP1 expression and that of NF-κB p105 (NFKB1) and NF-κB p100 (NFKB2) subunits (Fig. 4C). Based on the aforementioned findings that LUZP1 knockdown increased the sensitivity of HNSCC cells to DTX and CIS (Fig. 3B and C), validation of the contribution of NF-κB-LUZP1 signaling to chemoresistance was next sought. To this end, NF-κB p65

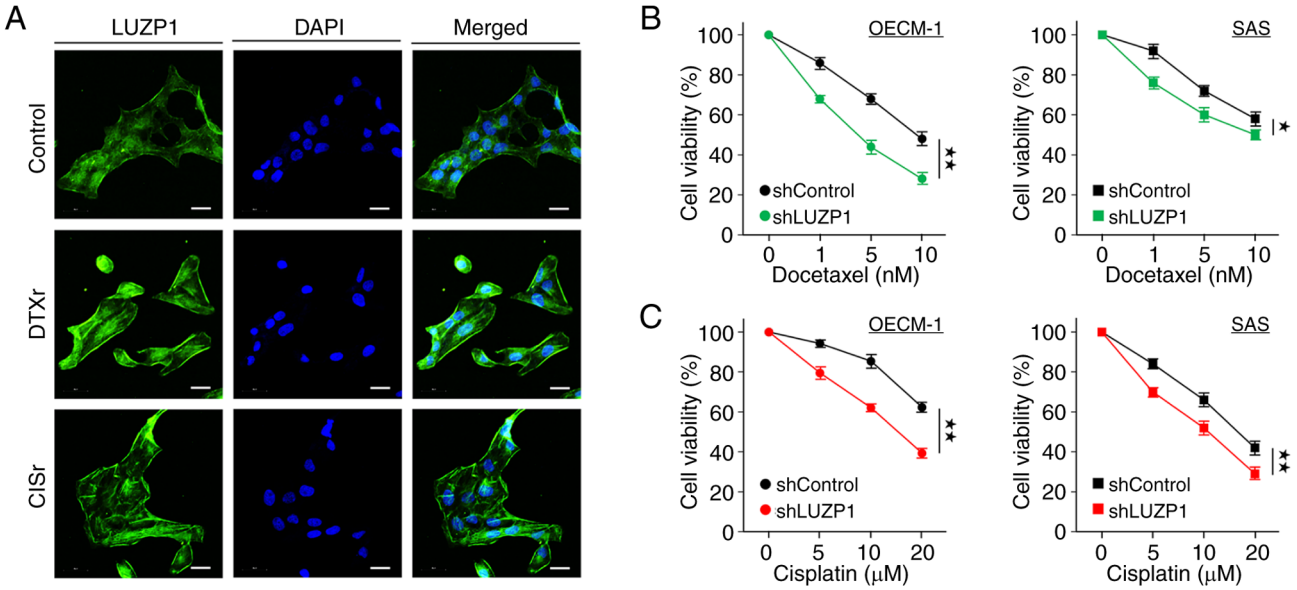

Figure 3. LUZP1 increases chemoresistance of head and neck squamous cell carcinoma cells. (A) Immunofluorescent analysis was conducted to examine LUZP1 expression in DTX-resistant, CIS-resistant and the control OECM-1 cells. Scale bar, 20 μm. Cell viability of OECM-1 and SAS with or without LUZP1 knockdown treated with the indicated doses of (B) DTX and (C) CIS was analyzed by MTT assay (n=3). For statistical analyses, (B and C) one-way ANOVA with Tukey's post hoc test. *P<0.05; **P<0.01. LUZP1, leucine zipper protein 1; sh, short hairpin; DTX, docetaxel; CIS, cisplatin.

was silenced using gene knockdown by shRNA. Western blot analysis showed that NF-κB knockdown resulted in a marked reduction of LUZP1 expression (Fig. 4D). Consistently, MTT assays demonstrated that NF-κB knockdown significantly enhanced the sensitivity of both OECM-1 and SAS cells to DTX and CIS, leading to a pronounced decrease in drug IC_{50} values (Fig. 4E and F). These results support that NF-κB-LUZP1 signaling may play a key role in mediating chemoresistance in HNSCC cells. To further validate the regulation of LUZP1 by NF-κB signaling, HNSCC cells were stimulated with the cytokines IL-1β and TNF-α, both known activators of NF-κB signaling (26). Western blot analysis showed that IL-1β and TNF-α both induced LUZP1 expression in a time-dependent manner (Fig. 4G and H). Moreover, to examine the functional consequences of NF-κB-mediated regulation of LUZP1, cell migration following LUZP1 knockdown and/or TNF-α stimulation was assessed. Using a two-way ANOVA to assess the effects of shLUZP1 and TNFα treatment, significant main effects of shLUZP1 ($F(1,8)=68.87$, $P=3.35\times10^{-5}$) and TNFα ($F(1,8)=216.30$, $P=4.49\times10^{-7}$) were observed, whereas the interaction term did not reach significant ($F(1,8)=0.026$, $P=0.877$) (Fig. 4I). Tukey's multiple comparisons post hoc test confirmed significant differences among all four groups (adjusted $P\leq0.01$). The results indicated that TNF-α treatment enhanced the migratory ability of parental HNSCC cells and effectively rescued the migration defect caused by LUZP1 knockdown (Fig. 4I).

To examine whether LUZP1 is transcriptionally regulated by NF-κB. An *in silico* analysis was first carried out to evaluate potential NF-κB-mediated regulation of the LUZP1 locus. Genomic snapshots of the human genome (GRCh38/hg38 assembly) spanning the LUZP1 region (Chr 1:23,082,260-23,191,800) were obtained from the UCSC Genome Browser (27). The resulting genomic visualization (Fig. 4J) integrates multiple regulatory features, including RefSeq-curated exon annotations (28) of LUZP1, NF-κB RelA ChIP-seq binding signals in FaDu cells from the ReMap database (29), and layered H3K27ac ChIP-seq profiles from several ENCODE cell lines (30), which mark active regulatory regions and are associated with transcriptional activation. Additionally, GeneHancer regulatory element annotations (31) were included, with red boxes denoting promoter regions and gray boxes indicating putative enhancers. Together, this analysis revealed potential NF-κB binding sites within the promoter and enhancer regions of LUZP1, suggesting a regulatory relationship between NF-κB and LUZP1 expression. Based on these sequence features, 10 sets of ChIP-qPCR primers were designed targeting candidate NF-κB-enriched regions (indicated by blue vertical bars in Fig. 4J) for experimental validation. ChIP-qPCR analysis demonstrated that TNF-α stimulation significantly enhanced NF-κB binding at the LUZP1 promoter (Fig. 4K), indicating that NF-κB occupancy at the LUZP1 promoter is inducible and context dependent. Collectively, these results demonstrate that the oncogenic roles of LUZP1 could be mediated through NF-κB signaling activation.

LUZP1 is associated with poor survival of patients with HNSCC. To assess the impact of LUZP1 on clinical outcomes, IHC assays were conducted in tissue specimens to determine the correlation between LUZP1 expression levels and OS and PFS in patients with HNSCC. A total of 130 pathologic specimens were collected from patients with HNSCC, with demographic information shown in Table I. Representative IHC staining images are shown in Fig. 5A. IHC signals were semi-quantitatively scored as 0, 1, 2 or 3, and a score ≥2 was defined as positive (LUZP1^{+}), as described in the Materials and methods section. The Kaplan-Meier plot analysis revealed that LUZP1^{+} was significantly associated with shorter OS and PFS in the present study cohort (Fig. 5B and C).

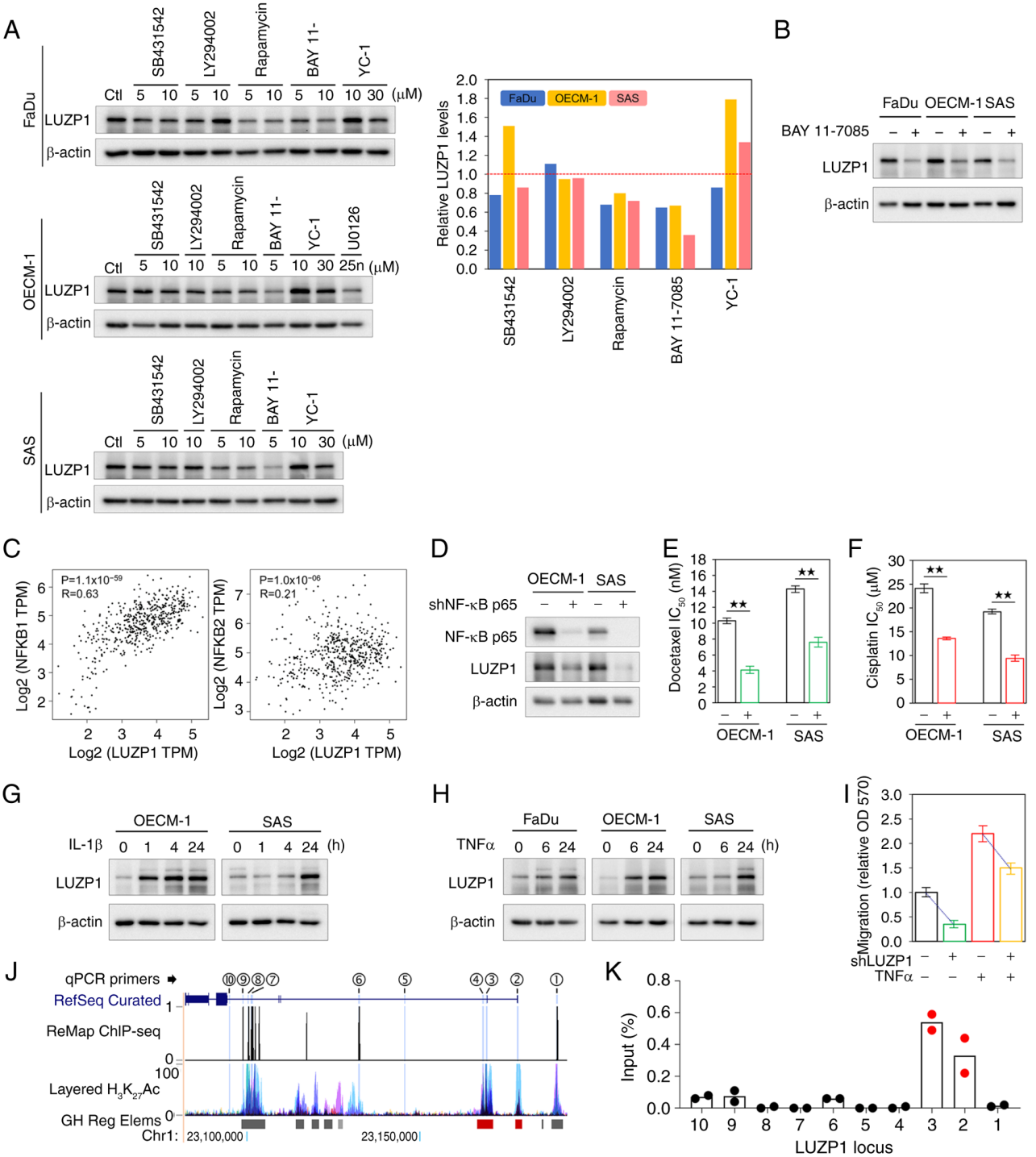

Figure 4. NF-κB signaling activation promotes LUZP1 expression in HNSCC cells. (A) The expression of LUZP1 in FaDu, OECM-1 and SAS cells treated with SB431542 (10 μM), LY294002 (10 μM), Rapamycin (10 μM), BAY 11-7085 (5 μM) or YC-1 (30 μM) was determined by western blot assay. Signal quantification was measured using ImageJ 1.54 g software (National Institutes of Health) and the relative intensity was normalized to untreated control. The red dashed line represents the normalized value as 1. (B) The expression of LUZP1 in FaDu, OECM-1 and SAS cells with or without BAY 11-7085 was validated by western blot assay. (C) Spearman's monotonic correlation between LUZP1 and NFKB1 or NFKB2 expression in HNSCC was analyzed using The Cancer Genome Atlas RNA-Sequencing database on the GEPIA server. (D) Protein expression of NF-κB p65 and LUZP1 in OECM-1 and SAS cells with NF-κB p65 knockdown (+) or control shRNA -), as determined by western blot analysis. β-actin, loading control. (E) IC_{50} values of docetaxel in OECM-1 and SAS cells with or without NF-κB p65 knockdown. (F) IC_{50} values of cisplatin in OECM-1 and SAS cells with or without NF-κB p65 knockdown. The expression of LUZP1 in different HNSCC cells treated with (G) IL-1β (3 ng/ml) or (H) TNFα (10 ng/ml) for the indicated times was determined by western blot assay. β-actin, loading control. (I) Transwell cell migration assay was conducted using OECM-1 cells with or without LUZP1 knockdown in the presence or absence of TNFα (10 ng/ml) treatment. Signal quantification using crystal violet extract was measured by colorimetric analysis at 570 nm, and the relative signal intensities were normalized to untreated shControl (shLUZP1, -; TNFα, -) (n=3). (J) Genomic visualization of the human LUZP1 locus (GRCh38/hg38) showing RefSeq-curated exon annotations, NF-κB RelA ChIP-seq binding signals in FaDu cells (ReMap), layered H3K27ac ChIP-seq profiles from ENCODE cell lines, and GeneHancer regulatory element annotations. Red boxes denote promoter regions and gray boxes indicate putative enhancers. Blue vertical bars mark the locations of ChIP-qPCR primer sets designed for experimental validation. (K) ChIP-qPCR analysis showing increased NF-κB (RelA) occupancy at the LUZP1 promoter in response to TNF-α treatment. For statistical analyses, (E and F) a 2-tailed unpaired Student's *t*-test; (I) a factorial two-way ANOVA, followed by Tukey's Honestly Significant Difference post hoc test. **P<0.01. TPM, transcripts per million; ChIP-seq, chromatin immunoprecipitation sequencing; LUZP1, leucine zipper protein 1; sh, short hairpin.

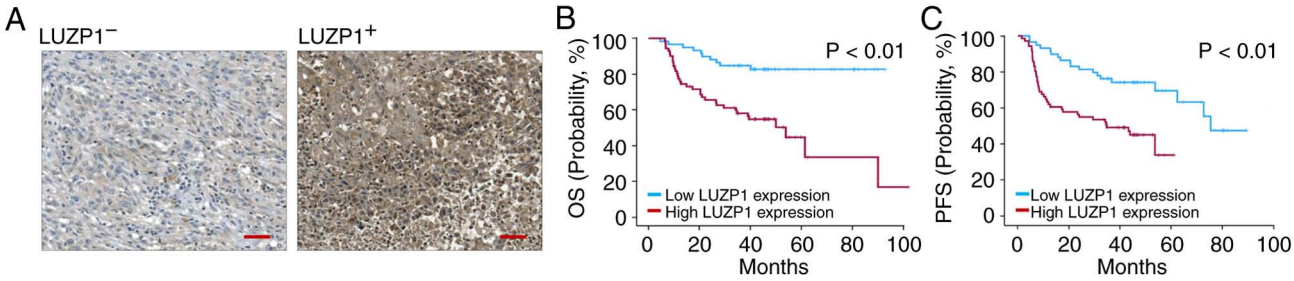

Figure 5. LUZP1 is associated with poor survival of patients with head and neck squamous cell carcinoma. (A) Representative immunohistochemical images demonstrating weak LUZP1 signal (LUZP 1^{-}; a score=0 or 1) and strong LUZP1 signal (LUZP 1^{+}; score=2 or 3) in pathologic specimens of patients with HNSCC. Correlations between LUZP1 expression and (B) OS or (C) PFS were analyzed according to LUZP1 signals using the Kaplan-Meier method. For statistical analyses, (B and C) log-rank test. OS, overall survival; PFS, progression free survival; LUZP1, leucine zipper protein 1; ChIP-seq, chromatin immunoprecipitation sequencing.

To determine whether LUZP1 expression independently predicts patient outcomes, multivariate Cox proportional hazards regression analyses were conducted with adjustment for age, T stage, nodal status, lymphovascular invasion (LVI), tumor differentiation, perineural invasion (PNI) and surgical margin status. High LUZP1 expression emerged as an independent prognostic factor for both OS and PFS (Tables II and III). Specifically, patients with high LUZP1 expression exhibited a significantly increased risk of mortality (OS; HR, 1.789-6.006; P<0.001) and disease progression or recurrence (PFS; HR, 2.202-9.924; P<0.001), independent of established clinicopathological variables. By contrast, tumor differentiation, LVI, PNI and surgical margin status did not retain independent prognostic significance for either OS or PFS in the multivariate models. In multivariate Cox regression analyses (Tables II and III), advanced nodal disease (N3) remained significantly associated with worse survival outcomes. Specifically, N3 was independently associated with reduced overall survival compared with N0 (Table II, P=0.029; Table III, P=0.004). Importantly, the prognostic impact of LUZP1 expression persisted after adjustment for nodal status and tumor stage, indicating that LUZP1 provides prognostic information beyond conventional staging parameters.

Discussion

HNSCC is a biologically and clinically heterogeneous malignancy and its poor prognosis is frequently driven by local recurrence, distant metastasis and therapeutic resistance despite the availability of multimodal treatment approaches. Identifying molecular determinants of poor survival is therefore essential for risk stratification and therapeutic guidance. The present study suggests that LUZP1 functions as a key oncogenic regulator in HNSCC, associating its expression with metastatic potential and chemoresistance through NF-κB signaling activation. Notably, IHC analysis of a patient cohort revealed that high LUZP1 expression was significantly associated with shorter OS and PFS, suggesting its potential utility as a prognostic biomarker.

LUZP1 was initially identified as an essential regulator of embryonic development, as *Luzp1*-null mice display neural tube closure defects and cardiovascular abnormalities that result in perinatal lethality (11). Subsequent studies have shown that LUZP1 functions as an actin-stabilizing protein and a negative regulator of ciliogenesis (32), and it has also been implicated in cell division, cell migration and epithelial apical constriction (9). In Townes-Brocks syndrome, a mechanistic study demonstrated that truncated SALL1 promotes proteasomal degradation of LUZP1, thereby associating LUZP1 deficiency with impaired cilia regulation and providing a direct pathway by which LUZP1 abnormality contributes to disease (33). Consistently, diseases associated with LUZP1 deficiency predominantly affect organs that depend on proper cytoskeletal dynamics and ciliary function, aligning with its established molecular roles in actin stabilization, inhibition of ciliogenesis and regulation of cell architecture and motility.

Accumulating evidence indicates that LUZP1 exerts context-dependent functions in cancer, yet its effects consistently converge on the regulation of cytoskeletal dynamics, cell migration and EMT-associated phenotypes (9,10). In glioma, deletions or loss of LUZP1 function have been associated with enhanced migration and invasion, likely through disruption of actin organization, cell division and polarity control, underscoring its role in maintaining cytoskeletal integrity (34). By contrast, a study in triple-negative breast cancer demonstrate that LUZP1 can heterodimerize with DAPK3, protecting it from proteasomal degradation and thereby indirectly promote EMT, desmosome suppression and invasive behavior (13). Similarly, in osteosarcoma, LUZP1 acts as a downstream effector of circFIRRE-miRNA regulatory circuits, facilitating tumor progression, angiogenesis and metastatic dissemination (12). Consistent with these reports, the functional analyses of the present study show that LUZP1 knockdown markedly suppresses migration and invasion of HNSCC cells, reduces invadopodia-like protrusive structures and prevents EMT-associated marker expression, as evidenced by E-cadherin upregulation and vimentin downregulation. Moreover, the observation that LUZP1 expression is elevated in metastatic lesions compared with matched primary tumors further supports its involvement in metastatic dissemination. Collectively, these findings suggest that although LUZP1 is not a canonical EMT transcription factor, it may function as an EMT-enabling factor by modulating actin cytoskeleton organization, actomyosin contractility and cellular plasticity.

Importantly, the EMT-associated plasticity driven by LUZP1 also provides a mechanistic basis for its contribution to drug resistance. KEGG pathway analysis of proteins upregulated in short-term survival tissues revealed significant enrichment of drug metabolism and glutathione-associated

Table II. Multivariate Cox regression analysis of overall survival in patients with head and neck squamous cell carcinoma.

		95.0% CI	
Characteristics	P-value	Low	Upper
Age			
40-60 vs. <40	0.364	0.281	1.594
40-60 vs. >60	0.108	0.166	1.195
T	0.095		
T4 vs. T1	0.039	0.062	0.933
T4 vs. T2	0.045	0.186	0.981
T4 vs. T3	0.486	0.273	1.854
Nodal	0.012		
N3 vs. N0	0.029	0.135	0.896
N3 vs. N1	0.092	0.056	1.243
N3 vs. N2	0.433	0.601	3.279
LVI			
No vs. yes	0.138	0.841	3.471
Differentiation	0.210		
Well vs. moderate	0.918	0.495	1.884
Well vs. poor	0.101	0.166	1.172
PNI			
No vs. yes	0.099	0.895	3.602
Margin			
Free vs. positive	0.244	0.357	1.300
LUZP1			
Low vs. High	<0.001	2.202	9.924

T, tumor stage; N, nodal stage.

Table III. Multivariate Cox regression analysis of progression-free survival in patients with head and neck squamous cell carcinoma.

		95.0% CI	
Characteristics	P value	Low	Upper
Age			
40-60 vs. <40	0.395	0.672	2.740
40-60 vs. >60	0.160	0.244	1.263
T			
T4 vs. T1	0.424	0.250	1.791
T4 vs. T2	0.817	0.295	2.617
T4 vs. T3	0.731	0.436	3.264
Nodal			
N3 vs. N0	0.004	0.122	0.665
N3 vs. N1	0.120	0.164	1.231
N3 vs. N2	0.251	0.289	1.383
LVI			
No vs. Yes	0.133	0.870	2.856
Differentiation			
Well vs Moderate	0.924	0.562	1.886
Well vs. Poor	0.089	0.190	1.125
PNI			
No vs. Yes	0.639	0.639	2.074
Margin			
Free vs. Positive	0.835	0.591	1.917
LUZP1			
Low vs. High	<.001	1.789	6.006

T, tumor stage; NS, nodal stage; LUZP1, leucine zipper protein 1; PNI, perineural invasion; LVI, lymphovascular invasion.

pathways, both of which are associated with chemoresistance. In line with these findings, the present study experimentally confirmed that LUZP1 expression is markedly elevated in DTZr and CISr OECM-1 cell lines. Conversely, LUZP1 knockdown restored chemosensitivity in both OECM-1 and SAS cells, indicating a functional role for LUZP1 in sustaining resistant phenotypes. Chemoresistance in HNSCC is widely recognized as a multifactorial process involving drug sequestration, efflux, detoxification and activation of pro-survival signaling pathways (35). Data of the present study suggests that LUZP1 represents an integral component of this resistance network. Rather than directly regulating drug metabolism or efflux, LUZP1 may promote therapy tolerance by coordinating cytoskeletal remodeling with cellular stress-adaptive programs. Such remodeling could influence intracellular drug uptake or trafficking or functionally cooperate with antioxidant and metabolic pathways to buffer cytotoxic stress (36-38). In addition, the functional convergence of LUZP1 with inflammatory and stress-responsive signaling pathways, including NF-κB-associated programs, may further reinforce anti-apoptotic responses during treatment (39). Together, these observations support a model in which LUZP1 integrates EMT-associated plasticity, cytoskeletal adaptation and metabolic stress buffering to promote both metastatic progression and therapeutic resistance in aggressive HNSCC, highlighting its potential value as a predictive biomarker and therapeutic target for chemoresistant disease.

NF-κB is a central regulator of inflammatory signaling, tumor progression and therapeutic resistance in HNSCC (26). It controls the transcription of cytokines, survival factors and invasion-promoting proteins, thereby shaping a tumor microenvironment that favors malignant progression (40). The present study identified NF-κB signaling as a key upstream regulator of LUZP1 expression. Pharmacologic inhibition with BAY 11-7085 consistently produced the strongest suppression of LUZP1 across multiple HNSCC cell lines, whereas stimulation with IL-1β and TNF-α, two potent NF-κB activators, induced LUZP1 expression in a time-dependent manner and rescued the migration defect caused by LUZP1 knockdown. These findings suggest that LUZP1 is a novel NF-κB effector contributing to pro-metastatic and chemoresistant phenotypes. The importance of this axis is reinforced by research that shows IL-1β and TNF-α enhance EMT, stemness, migration, invasion and metastatic outgrowth through NF-κB-driven programs across multiple types of cancer (25,41-43). IL-1β acts via PI3K/AKT and

ZEB1-dependent pathways, while TNF-α stabilizes Snail to accelerate epithelial-mesenchymal plasticity, both converging on NF-κB activation. Collectively, the results of the present study indicate that the NF-κB-LUZP1 axis integrates inflammatory cytokine signaling with EMT and therapy resistance, representing a potential therapeutic vulnerability in HNSCC.

The present study has several limitations that should be acknowledged. Although the promotion of metastasis and chemoresistance by LUPZ1 is demonstrated, the precise molecular mechanisms remain to be clarified. Future investigations should delineate how LUZP1 interacts with cytoskeletal and metabolic networks at the molecular level. Furthermore, while NF-κB was identified as an upstream regulator of LUZP1, it remains uncertain whether additional signaling pathways also converge on its regulation. Given the complexity of HNSCC signaling, it is plausible that LUZP1 functions as an integrator of multiple oncogenic inputs. Finally, although BAY 11-7085 effectively suppressed LUZP1 expression *in vitro*, its clinical translation is limited by issues of toxicity and specificity. The development of more selective inhibitors or RNA-based therapeutic approaches may therefore be required to target LUZP1 effectively in the clinical setting.

In summary, the present study identifies LUZP1 as a key oncogenic regulator in HNSCC that associates poor survival with enhanced metastatic potential and chemoresistance. The present study demonstrated that elevated LUZP1 expression promotes EMT, invasion and drug resistance, and is significantly associated with shorter OS and PFS in patient cohorts. Mechanistically, LUZP1 expression is driven, at least in part, by NF-κB signaling and can be induced by pro-inflammatory cytokines such as IL-1β and TNF-α, thereby integrating inflammatory cues with tumor aggressiveness. These findings highlight LUZP1 not only as a potential prognostic biomarker but also as a candidate therapeutic target in HNSCC. Further studies are warranted to delineate the detailed molecular mechanisms of LUZP1 regulation and to explore therapeutic strategies for its clinical translation.

Acknowledgements

Not applicable.

Funding

No funding was received.

Availability of data and materials

All MS raw datasets generated in the present study have been deposited in the jPOST (44) and ProteomeXchange repositories. The accession numbers are JPST004371 for jPOST and PXD073924 for ProteomeXchange. The data will be publicly accessible starting on 2 Feb 2026 and can be previewed via the jPOST repository using the following link and access key: https://repository.jpostdb.org/preview/1096459080698079a08d66e (access key: 6669).

Authors' contributions

CYL, CYH, YAT and WCC conceived the present study. CYL, CYH, HCL, CCL, TTC and WCT performed the experiments. HCL, WCT and YAT analyzed the data. TTC and WCT confirm the authenticity of all the raw data. CYL, CYH, HCL, YAT and WCC wrote the manuscript. WCC revised the manuscript. All authors read and approved the final manuscript.

Ethics approval and consent to participate

The present study protocol was approved by the Ethics Committee of China Medical University Hospital (Taichung, Taiwan; approval no. CMUH108-REC1-127).

Patient consent for publication

Not applicable.

Competing interests

The authors declare that they have no competing interests.

References

1. Johnson DE, Burtness B, Leemans CR, Lui VWY, Bauman JE and Grandis JR: Head and neck squamous cell carcinoma. Nat Rev Dis Primers 6: 92, 2020.
2. Liu YP, Zheng CC, Huang YN, He ML, Xu WW and Li B: Molecular mechanisms of chemo- and radiotherapy resistance and the potential implications for cancer treatment. MedComm (2020) 2: 315-340, 2021.
3. Lee DY, Abraham J, Ross E, Ridge JA, Lango MN, Liu JC, Bauman JR, Avkshtol V and Galloway TJ: Rapid recurrence in head and neck cancer: Underappreciated problem with poor outcome. Head Neck 43: 212-222, 2021.
4. Shirima CA, Bleotu C, Spandidos DA, El-Naggar AK, Gradisteanu Pircalabioru G and Michalopoulos I: Epithelial-derived head and neck squamous tumourigenesis (Review). Oncol Rep 52: 141, 2024.
5. Duan XP, Qin BD, Jiao XD, Liu K, Wang Z and Zang YS: New clinical trial design in precision medicine: Discovery, development and direction. Signal Transduct Target Ther 9: 57, 2024.
6. Park R and Chung CH: Advanced human papillomavirus-negative head and neck squamous cell carcinoma: unmet need and emerging therapies. Mol Cancer Ther 23: 1717-1730, 2024.
7. Tathineni P, Joshi N and Jelinek MJ: Current state and future directions of EGFR-directed therapy in head and neck cancer. Curr Treat Options Oncol 24: 680-692, 2023.
8. Wang Y, Han J, Zhu Y, Huang N and Qu N: New advances in the therapeutic strategy of head and neck squamous cell carcinoma: A review of latest therapies and cutting-edge research. Biochim Biophys Acta Rev Cancer 1880: 189230, 2025.
9. Bozal-Basterra L, Gonzalez-Santamarta M, Muratore V, Martín-Martín N, Ercilla A, Rodríguez JA, Carracedo A, Sutherland JD and Barrio R: LUZP1 controls cell division, migration and invasion through regulation of the actin cytoskeleton. Front Cell Dev Biol 9: 624089, 2021.
10. Wang L, Tsang HY, Yan Z, Tojkander S, Ciuba K, Kogan K, Liu X and Zhao H: LUZP1 regulates the maturation of contractile actomyosin bundles. Cell Mol Life Sci 81: 248, 2024.
11. Hsu CY, Chang NC, Lee MW, Lee KH, Sun DS, Lai C and Chang AC: LUZP deficiency affects neural tube closure during brain development. Biochem Biophys Res Commun 376: 466-471, 2008.
12. Yu L, Zhu H, Wang Z, Huang J, Zhu Y, Fan G, Wang Y, Chen X and Zhou G: Circular RNA circFIRRE drives osteosarcoma progression and metastasis through tumorigenic-angiogenic coupling. Mol Cancer 21: 167, 2022.
13. Wang J, Tran-Huynh AM, Kim BJ, Chan DW, Holt MV, Fandino D, Yu X, Qi X, Wang J, Zhang W, *et al*: Death-associated protein kinase 3 modulates migration and invasion of triple-negative breast cancer cells. PNAS Nexus 3: pgae401, 2024.
14. Poel D, Boyd LNC, Beekhof R, Schelfhorst T, Pham TV, Piersma SR, Knol JC, Jimenez CR, Verheul HMW and Buffart TE: Proteomic analysis of miR-195 and miR-497 replacement reveals potential candidates that increase sensitivity to oxaliplatin in MSI/P53wt colorectal cancer cells. Cells 8: 1111, 2019.

15. Chen M, Wang J and Xiao Y: Leucine zipper protein 1 (LUZP1) serves as a prognostic biomarker for patients with renal papillary cell carcinoma. Asian J Surg 46: 4011-4013, 2023.
16. Yu D, Luo Y, Guo R, Ma F, Chang Y and Dang J: Comprehensive profiling of endocrine metabolism identifies a novel signature with robust predictive value in ovarian cancer. J Gene Med 26: e3686, 2024.
17. Chandrashekar DS, Karthikeyan SK, Korla PK, Patel H, Shovon AR, Athar M, Netto GJ, Qin ZS, Kumar S, Manne U, *et al*: UALCAN: An update to the integrated cancer data analysis platform. Neoplasia 25: 18-27, 2022.
18. Li C, Tang Z, Zhang W, Ye Z and Liu F: GEPIA2021: integrating multiple deconvolution-based analysis into GEPIA. Nucleic Acids Res 49(W1): W242-W246, 2021.
19. Schmittgen TD, and Livak KJ: Analyzing real-time PCR data by the comparative C(T) method. Nat Protoc 3: 1101-1108, 2008.
20. Tung JC, Huang WC, Yang JC, Chen GY, Fan CC, Chien YC, Lin PS, Candice Lung SC and Chang WC: Auramine O, an incense smoke ingredient, promotes lung cancer malignancy. Environ Toxicol 32: 2379-2391, 2017.
21. Espina JA, Cordeiro MH, Milivojevic M, Pajić-Lijaković I and Barriga EH: Response of cells and tissues to shear stress. J Cell Sci 136: jcs260985, 2023.
22. Hsieh CY, Lin CC and Chang WC: Taxanes in the treatment of head and neck squamous cell carcinoma. Biomedicines 11: 2887, 2023.
23. Franken NA, Rodermond HM, Stap J, Haveman J and van Bree C: Clonogenic assay of cells in vitro. Nat Protoc 1: 2315-2319, 2006.
24. Fan CC, Cheng WC, Huang YC, Sher YP, Liou NJ, Chien YC, Lin PS, Lin PS, Chen CH and Chang WC: EFHD2 promotes epithelial-to-mesenchymal transition and correlates with post-surgical recurrence of stage I lung adenocarcinoma. Sci Rep 7: 14617, 2017.
25. Hsieh CY, Lin CC, Huang YW, Chen JH, Tsou YA, Chang LC, Fan CC, Lin CY and Chang WC: Macrophage secretory IL-1β promotes docetaxel resistance in head and neck squamous carcinoma via SOD2/CAT-ICAM1 signaling. JCI Insight 7: e157285, 2022.
26. Liu T, Zhang L, Joo D and Sun SC: NF-κB signaling in inflammation. Signal Transduct Target Ther 2: 17023, 2017.
27. Casper J, Speir ML, Raney BJ, Perez G, Nassar LR, Lee CM, Hinrichs AS, Gonzalez JN, Fischer C, Diekhans M, *et al*: The UCSC genome browser database: 2026 update. Nucleic Acids Res 54: D1331-D1335, 2026.
28. Pruitt KD, Brown GR, Hiatt SM, Thibaud-Nissen F, Astashyn A, Ermolaeva O, Farrell CM, Hart J, Landrum MJ, McGarvey KM, *et al*: RefSeq: An update on mammalian reference sequences. Nucleic Acids Res 42: D756-D763, 2014.
29. Hammal F, de Langen P, Bergon A, Lopez F and Ballester B: ReMap 2022: A database of Human, Mouse, Drosophila and Arabidopsis regulatory regions from an integrative analysis of DNA-binding sequencing experiments. Nucleic Acids Res 50: D316-D325, 2022.
30. Moore JE, Pratt HE, Fan K, Phalke N, Fisher J, Elhajjajy SI, Andrews G, Gao M, Shedd N, Fu Y, *et al*: An expanded registry of candidate cis-regulatory elements. Nature: Jan 7, 2026 (Epub ahead of print).
31. Fishilevich S, Nudel R, Rappaport N, Hadar R, Plaschkes I, Iny Stein T, Rosen N, Kohn A, Twik M, Safran M, *et al*: GeneHancer: Genome-wide integration of enhancers and target genes in GeneCards. Database (Oxford) 2017: bax028, 2017.
32. Gonçalves J, Sharma A, Coyaud É, Laurent EMN, Raught B and Pelletier L: LUZP1 and the tumor suppressor EPLIN modulate actin stability to restrict primary cilia formation. J Cell Biol 219: e201908132, 2020.
33. Bozal-Basterra L, Gonzalez-Santamarta M, Muratore V, Bermejo-Arteagabeitia A, Da Fonseca C, Barroso-Gomila O, Azkargorta M, Iloro I, Pampliega O, Andrade R, *et al*: LUZP1, a novel regulator of primary cilia and the actin cytoskeleton, is a contributing factor in Townes-Brocks Syndrome. Elife 9: e55957, 2020.
34. Dong X, Zhang P, Liu L, Li H, Cheng S, Li S, Wang Y, Zheng C, Dong J and Zhang L: The Circ_0001367/miR-545-3p/LUZP1 axis regulates cell proliferation, migration and invasion in glioma cells. Front Oncol 11: 781471, 2021.
35. Khera N, Rajkumar AS, Abdulkader M Alkurdi K, Liu Z, Ma H, Waseem A and The MT: Identification of multidrug chemoresistant genes in head and neck squamous cell carcinoma cells. Mol Cancer 22: 146, 2023.
36. DeWane G, Salvi AM and DeMali KA: Fueling the cytoskeleton-links between cell metabolism and actin remodeling. J Cell Sci 134: jcs248385, 2021.
37. Aseervatham J: Cytoskeletal Remodeling in Cancer. Biology (Basel) 9: 385, 2020.
38. Song Z, Cui Y, Xin L, Xiao R, Feng J, Li C, Yin Z, Wang H, Li Q, Wang M, *et al*: Mechano-oncogenic cytoskeletal remodeling drives leukemic transformation with mitochondrial vesicle-mediated STING activation. Cell Stem Cell 32: 581-597.e11, 2025.
39. Mao H, Zhao X and Sun SC: NF-κB in inflammation and cancer. Cell Mol Immunol 22: 811-839, 2025.
40. Cao Y, Yi Y, Han C and Shi B: NF-κB signaling pathway in tumor microenvironment. Front Immunol 15: 1476030, 2024.
41. Liu C, Wu K, Li C, Zhang Z, Zhai P, Guo H and Zhang J: SPP1+ macrophages promote head and neck squamous cell carcinoma progression by secreting TNF-α and IL-1β. J Exp Clin Cancer Res 43: 332, 2024.
42. Rébé C and Ghiringhelli F: Interleukin-1β and cancer. Cancers (Basel) 12: 1791, 2020.
43. Chen S, Yang Y, Zheng Z, Zhang M, Chen X, Xiao N and Liu H: IL-1β promotes esophageal squamous cell carcinoma growth and metastasis through FOXO3A by activating the PI3K/AKT pathway. Cell Death Discov 10: 238, 2024.
44. Okuda S, Yoshizawa AC, Kobayashi D, Takahashi Y, Watanabe Y, Moriya Y, Hatano A, Takami T, Matsumoto M, Araki N, *et al*: jPOST environment accelerates the reuse and reanalysis of public proteome mass spectrometry data. Nucleic Acids Res 53: D462-D467, 2025.